Ultrasensitive optical imaging with lanthanide lumiphores

Ukrae Cho[1], Daniel P Riordan[2,4], Paulina Ciepla[1], Kiranmai S Kocherlakota[1,4], James K Chen[1,3]*
& Pehr B Harbury[2]*

In principle, the millisecond emission lifetimes of lanthanide chelates should enable their ultrasensitive detection in biological systems by time-resolved optical microscopy. In practice, however, lanthanide imaging techniques have provided no better sensitivity than conventional fluorescence microscopy. Here, we identified three fundamental problems that have impeded lanthanide microscopy: low photon flux, inefficient excitation, and optics-derived background luminescence. We overcame these limitations with a new lanthanide imaging modality, transreflected illumination with luminescence resonance energy transfer (trLRET), which increases the time-integrated signal intensities of lanthanide lumiphores by 170-fold and the signal-to-background ratios by 75-fold. We demonstrate that trLRET provides at least an order-of-magnitude increase in detection sensitivity over that of conventional epifluorescence microscopy when used to visualize endogenous protein expression in zebrafish embryos. We also show that trLRET can be used to optically detect molecular interactions *in vivo*. trLRET promises to unlock the full potential of lanthanide lumiphores for ultrasensitive, autofluorescence-free biological imaging.

The ability to image molecular features within complex biological samples has improved dramatically over the past two decades. Synthetic and genetically encoded fluorescent probes with enhanced extinction coefficients and quantum yields have been developed[1,2], far-red-fluorescent proteins have extended the spectral range of molecular imaging[3,4], and hybrid tandem fluorophores have facilitated single-molecule detection[5–8]. Yet molecules expressed at nanomolar or lower concentrations are still difficult to detect optically in cells and whole organisms. Weak probe signals are often overwhelmed by the autofluorescence associated with flavins, hemes, and other metabolites with conjugated-π systems. Biological specimens treated with aldehyde crosslinking agents can also exhibit fixation-induced fluorescence to varying extents.

One promising approach for overcoming the autofluorescence of biological samples is the use of probes with long-lived photoluminescence. Lanthanide lumiphores have emission lifetimes in the millisecond regime, whereas those of biological fluorophores are typically less than 10 ns. Consequently, lanthanide-emitted photons can be differentiated from biological autofluorescence through pulsed excitation and time-delayed signal acquisition[9,10] (**Supplementary Results**, **Supplementary Fig. 1**). Since the development of time-resolved luminescence microscopes in the early 1990s[11–14], dozens of lanthanide chelates have been synthesized for molecular imaging and metabolite sensing[15–19]. These complexes exhibit large Stokes shifts, narrow emission bands, photostability, and resistance to oxygen-mediated quenching. Solid-state pulsed-light sources and intensified charge-coupled device (ICCD) cameras with single-photon sensitivity and submicrosecond gating have also improved the capabilities of time-resolved microscopy.

Despite these advances, lanthanide probes are still not widely used for biological imaging. Lanthanide imaging systems have not previously achieved the signal intensities and detection sensitivities required for routine applications, and they have not surpassed the capabilities of conventional fluorescence microscopy. These aspects are paradoxical, given the predominance of lanthanide probes in ultrasensitive solution- and cell-based photometric assays[20–22]. Here, we identified and solved three problems that have limited current lanthanide imaging systems. First, the millisecond excited-state lifetimes of lanthanides result in low photon flux and imaging rates, thus limiting their utility for biological microscopy. Second, the light-emitting diodes (LEDs) typically used for lanthanide imaging[10,23] excite only a small fraction of lanthanide probe within each imaging cycle, and this excitation efficiency decreases further as lanthanide emission rates increase. Third, the potential gains in the signal-to-noise ratio achieved by suppression of the autofluorescence background are bounded by long-lived luminescence within the microscope objective lenses. This optics-derived luminescence is spectrally and temporally difficult to differentiate from lanthanide-probe luminescence[24], and it degrades the signal-to-background ratios of the resulting images. In quantitative terms, a cutting-edge time-resolved microscope (equipped with a UV LED excitation source, an ICCD camera, and optimized emission filters[24]) achieves signal-to-background ratios of ~7 when cells containing 1–10 μM lanthanide probe are imaged[25]. Thus, current lanthanide imaging technologies cannot surpass conventional fluorescence microscopy.

To address each of the challenges cited above, we developed a new modality for time-resolved lanthanide imaging. Our approach, termed trLRET, uses spectrally matched acceptor molecules to tune the emission rates and wavelengths of lanthanide lumiphores. In parallel, we used Q-switched laser (QSL) illumination to dramatically increase the lanthanide excitation rates and consequently the excited-state fraction for each imaging cycle. In combination, these imaging modalities boost lanthanide-dependent signal intensities by 170-fold while still suppressing biological autofluorescence through temporal filtering. We also used transillumination and UV-light-reflecting coverslips to minimize optics-derived photoluminescence, thereby improving probe detection sensitivities by 75-fold. Using lanthanide-chelate-functionalized antibodies and diffusion-mediated LRET, we were able to image endogenous proteins in zebrafish embryos with detection sensitivities and

[1]Department of Chemical and Systems Biology, Stanford University School of Medicine, Stanford, California, USA. [2]Department of Biochemistry, Stanford University School of Medicine, Stanford, California, USA. [3]Department of Developmental Biology, Stanford University School of Medicine, Stanford, California, USA. [4]Present addresses: 10X Genomics, Pleasanton, California, USA (D.P.R.), and Chan-Zuckerberg Biohub and Department of Bioengineering, Stanford University School of Engineering, Stanford, California, USA (K.S.K.). *e-mail: jameschen@stanford.edu or harbury@stanford.edu

signal-to-background ratios exceeding those possible with conventional fluorophores. We were also able to exploit proximity-dependent changes in LRET efficiency to visualize molecular interactions *in vivo*. Thus, trLRET opens the door to a new realm of ultrasensitive optical microscopy.

RESULTS

Identification of a lanthanide complex for *in vivo* imaging

To increase brightness, lanthanide cations are typically complexed with a multidentate ligand bearing an energetically matched chromophore (commonly referred to as an 'antenna')[26]. Energy transferred from the excited antenna to the metal ion can then be dissipated through photon emission or nonradiative decay. Among the 15 lanthanides, Eu^{3+}, Gd^{3+}, and Tb^{3+} have electronic states that favor radiative pathways, with maximum emissions centered at red, ultraviolet, and green wavelengths, respectively[27]. Eu^{3+} complexes are best suited for biological applications because they can be excited by longer, less cytotoxic wavelengths of light (>350 nm), and numerous organic ligands have been synthesized, including members of the EDTA, DTPA, TTHA, DOTA, triazacyclononane, terpyridine, and cryptand families[19,28,29]. Structurally diverse antennae have also been developed, such as coumarins, azaxanthones, acridones, 1-hydroxypyridin-2-ones, and tetraazatriphenylene.

Many of these luminescent Eu^{3+} complexes have subfemtomolar dissociation constants in aqueous solutions[30]; however, the chelates can be sensitive to metabolites commonly found in cells. For example, trivalent lanthanide ions are efficiently sequestered by nucleoside triphosphates (NTPs and dNTPs) and inorganic phosphates[31]. Lanthanide luminescence can also be quenched by electron-rich metabolites such as ascorbate and urate[16]. We therefore sought to identify Eu^{3+} complexes that might be appropriate for *in vivo* applications, focusing on the readily synthesized Eu^{3+}–cs124-CF$_3$ ligand[32] and commercially available ATBTA[33]. We observed that Eu^{3+}–ATBTA is considerably less sensitive to dNTPs and ascorbate-mediated quenching than Eu^{3+}–DTPA–cs124-CF$_3$ (**Supplementary Fig. 2**), perhaps because of the ability of the ATBTA ligand to engage all nine metal-ion-coordination sites and sterically block collisional quenching. We evaluated the Eu^{3+}–ATBTA chelate *in vivo* by coupling it to a morpholino oligonucleotide (MO) via cyanuric chloride and injecting the resulting Eu^{3+}–DTBTA-functionalized reagent into zebrafish zygotes. The embryos were then imaged with a time-resolved epifluorescence microscope equipped with a 365-nm LED source, an ICCD camera, and a programmable digital delay generator[24,34]. The Eu^{3+}–DTBTA–MO–injected zygotes developed normally and exhibited long-lived Eu^{3+} emission signals for more than 3 d (**Supplementary Fig. 3**), thus demonstrating the efficacy of Eu^{3+}–DTBTA-based probes for biological applications.

LRET-accelerated lanthanide emission

Although the millisecond-scale luminescence lifetimes of lanthanide complexes enable the temporal filtering of autofluorescence, they also cause the emission rates to be 100,000-fold lower than that for typical organic fluorophores, which have fluorescence lifetimes in the single-digit nanosecond scale. This slow emission severely limits the brightness of lanthanide lumiphores, and numerous imaging cycles are typically required to obtain adequate signal intensities. This timescale is generally acceptable for photometric assays, such as those using microplate formats. However, the multiple seconds required to collect a time-resolved micrograph (<1 kHz and 10^3–10^5 integrated cycles per image) match or exceed the timescales of many biological processes.

Lanthanide probes with excited-state lifetimes in the 0.1- to 10-μs regime would still enable time-gated removal of background autofluorescence and greatly increase photon output per unit time. We hypothesized that this goal could be realized by pairing luminescent lanthanide complexes with spectrally matched acceptors
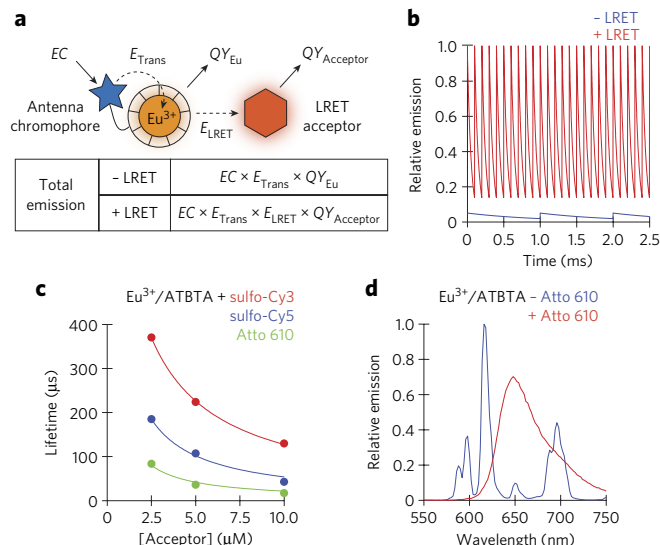
Figure 1 | Time-resolved lanthanide detection and LRET enhancement. (**a**) Energy cascades involved in direct Eu^{3+}-chelate and LRET emissions. E_{LRET} is given by $1 - \tau_{+LRET}/\tau_{-LRET}$. E, efficiency; QY, quantum yield; EC, extinction coefficient. (**b**) Emission-rate profiles associated with conventional (blue; $\tau = 1,000$ μs and pulse interval = 1,000 μs) and LRET-enhanced (red; $\tau = 50$ μs and pulse interval = 100 μs) time-resolved microscopy, assuming equivalent total emissions for each excited state. (**c**) Concentration-dependent decrease in Eu^{3+}–ATBTA emission lifetimes by spectrally distinct LRET acceptors (sulfo-Cy3, sulfo-Cy5, and Atto 610; 1 μM Eu^{3+}–ATBTA). The data were fit to a diffusion-enhanced LRET model (Online Methods), thus yielding R^2 values of 1.00, 0.987, and 0.973, respectively. (**d**) Emission spectra of 1 μM Eu^{3+}–ATBTA in the presence or absence of 10 μM Atto 610.

(**Fig. 1a,b** and **Supplementary Fig. 1**). The resulting LRET would bypass the parity-forbidden *f*–*f* atomic-orbital transition to the lanthanide ground state, thereby creating an alternative radiative pathway with faster kinetics and therefore shorter excited-state lifetimes. Like fluorescence resonance energy transfer, LRET can be achieved through the structural juxtaposition of lanthanide donors and acceptor fluorophores. Alternatively, freely diffusible acceptors can come within one Förster radius of a lanthanide donor during its excited-state lifetime and undergo energy transfer[35].

Using photometric measurements of homogenous solutions, we examined how the Eu^{3+}–ATBTA excited-state lifetime was affected by three potential LRET acceptors: Atto 610, sulfo-Cy5, and sulfo-Cy3. Each of the fluorophores decreased the average Eu^{3+}–ATBTA excited-state lifetime in a concentration-dependent manner, in proportion to its spectral overlap with the 614-nm emission line of the Eu^{3+}–ATBTA complex (**Fig. 1c,d** and **Supplementary Fig. 4**). Atto 610, which has a 615-nm excitation maximum and a 633-nm emission maximum, was the most efficient acceptor. A 10-μM concentration of this acceptor increased the decay rate of excited Eu^{3+}–ATBTA by 60-fold (lifetime $\tau = 1,020$ μs (ref. 33) versus 17 μs), thus leading to LRET luminescence with a 633-nm emission maximum. In addition, the greater quantum yield of Atto 610 in comparison to the Eu^{3+}–ATBTA complex (70% versus 38%; Online Methods) resulted in a 1.8-fold signal enhancement (**Fig. 1a**). Thus, lanthanide complexes can be tuned to shorter excited-state lifetimes by controlling the spectral properties and local concentrations of fluorescence acceptors.

LRET-enhanced time-resolved lanthanide microscopy

We next investigated whether LRET could be used to increase the signal intensities of lanthanide probes during time-resolved microscopy (as depicted in **Fig. 1b**). We immobilized Eu^{3+}–ATBTA onto agarose

beads and immersed the resin in an aqueous solution with or without Atto 610. Using pulsed LED illumination, we observed average excited-state lifetimes of 36.0 ± 0.5 μs and 951 ± 41 μs, respectively, for the two conditions (**Fig. 2a,b**). We then imaged direct lanthanide emissions from the Eu³⁺–ATBTA-conjugated beads by using 1,500 imaging cycles at 450 Hz, each including a 1-μs excitation, a 1-μs delay, and a 2-ms signal acquisition time. Emissions in the presence of 10 μM Atto 610 were similarly detected with 60,000 imaging cycles at 18,000 Hz, each including a 1-μs excitation, a 1-μs delay, and a 50-μs signal acquisition time. The two protocols had identical total acquisition and imaging times (3 s and 3.3 s, respectively; **Fig. 2c**), and we used a 575-nm long-pass emission filter to simultaneously capture Eu³⁺–ATBTA and Atto 610 emissions. The application of 1-μs LED pulses in both protocols also ensured that comparable excited-state levels were attained for each imaging cycle (described below).

On the basis of the intrinsic and LRET-tuned lifetimes for the excited Eu³⁺–ATBTA-conjugated beads and our emission acquisition parameters, the addition of Atto 610 should have increased the integrated lanthanide-probe signal by 29-fold. The higher quantum yield of the LRET acceptor was expected to improve this increase further and to result in a 52-fold enhancement in luminescence intensity. In line with this expectation, the LRET-enhanced images exhibited pixel intensities 50-fold greater than those obtained by time-resolved microscopy without LRET enhancement (**Fig. 2c**).

LED illumination limits lanthanide excitation rates

The photoluminescence of lanthanide probes is influenced not only by their emission kinetics but also by their excitation rates. Signal intensities are proportional to the fraction of lumiphores that are excited in each imaging cycle, which itself is a function of the excitation and emission rate constants (k_{ex} and k_{em}, respectively) and illumination time (**Supplementary Fig. 5**). In the case of LRET-enhanced lanthanide detection, k_{ex} is dependent on the light source and donor structure, and k_{em} varies with acceptor structure and concentration. Under these conditions, the excited-state fraction initially increases with longer excitation pulses. As the pulse width approaches the average excited-state lifetime ($\tau_{em} = 1/k_{em}$), the number of excited lanthanide probes begins to plateau with a steady-state maximum corresponding to $k_{ex}/(k_{ex} + k_{em})$.

We sought to determine the lanthanide excitation rate that could be achieved with an LED source, the standard illumination method for time-resolved lanthanide microscopy. We imaged Eu³⁺–ATBTA-conjugated agarose beads with LED pulses of varying duration, in the absence or presence of 10 μM Atto 610 (**Fig. 2d,e**). For these studies, we decreased the level of Eu³⁺–ATBTA labeling on the agarose beads so that we could survey a broad range of excitation-pulse widths (10 μs to 2 ms). Direct Eu³⁺–ATBTA luminescence increased steadily with pulse width and began to plateau as excitation pulses exceeded 500 μs in length. In contrast, photoluminescence from Atto 610–treated Eu³⁺–ATBTA beads reached a steady-state maximum that was approximately 20-fold lower in intensity. By combining these observations with our empirically measured average excited-state lifetimes (**Fig. 2a,b**), we determined the excitation rate constant k_{ex} to be 357 s⁻¹.

On the basis of these findings, 25% of the Eu³⁺–ATBTA complexes were in their excited state during continuous LED illumination (**Fig. 2f**). This steady-state population decreased to 1.3% when 10 μM Atto 610 acceptor was added. By extrapolation, the excited-state fraction of Eu³⁺–ATBTA would be 0.035% if a 1-μs LED pulse width were applied in the presence of 10 μM Atto 610, thereby negating the signal-intensity enhancement afforded by faster emission rates and shorter imaging cycles. Thus, standard LEDs have insufficient radiant flux to realize the full potential of LRET-enhanced lanthanide imaging, and pulsatile light sources with greater photon flux are necessary.
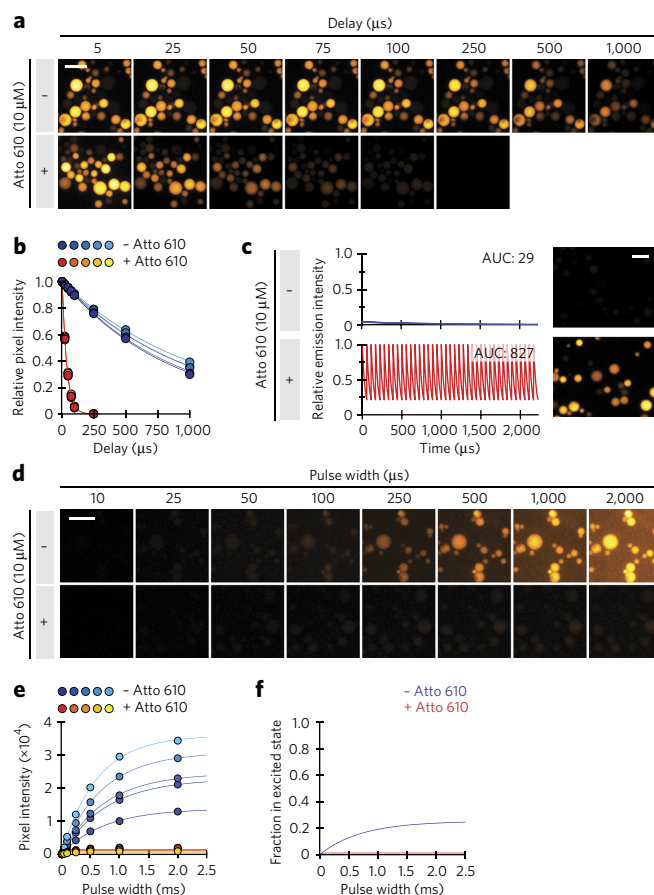

Figure 2 | LRET-enhanced time-resolved imaging of lanthanide-functionalized beads. (**a**) Time-resolved images of Eu³⁺–ATBTA-functionalized beads in the absence or presence of 10 μM Atto 610. Each imaging cycle included a 10-μs excitation pulse, the indicated delay, and a 500-μs emission acquisition period. (**b**) Average pixel intensities of five representative beads in **a**. The data were fit to a first-order decay model to obtain emission lifetimes for the immobilized Eu³⁺–ATBTA in the absence or presence of 10 μM Atto 610 of 951 ± 41 μs and 36.0 ± 0.5 μs, respectively (error, s.e.m.; $n = 5$ beads). Scale bar, 200 μm. (**c**) Comparison of conventional and LRET-enhanced time-resolved imaging of Eu³⁺–ATBTA-functionalized beads. Total imaging time was identical for each condition, with individual cycles including a 1-μs excitation pulse, 1-μs delay, and either a 2,000-μs (− Atto 610) or 50-μs (+ Atto 610) acquisition period. Emission curves were plotted assuming identical quantum yields for direct and LRET-mediated photoluminescence, and area under the curve (AUC) values are shown. The mean pixel intensities of the two micrographs were 45 (− Atto 610) and 2,239 (+ Atto 610). Scale bar, 200 μm. (**d**) Lanthanide lumiphore excitation saturates at less than 2% in the presence of an LRET acceptor, thus demonstrating the limitations of LED illumination. Eu³⁺–ATBTA-functionalized beads were imaged by time-resolved microscopy with varying illumination pulse widths. Micrographs of beads imaged in the absence or presence of 10 μM Atto 610 are shown. Scale bar, 200 μm. (**e**) Average pixel intensities for five representative beads in **d**. The data were fit to the equation in **Supplementary Figure 5** to determine an LED-induced excitation rate (k_{ex}) of 357 ± 56 s⁻¹ (error, s.e.m.; $n = 5$ beads). (**f**) Predicted excitation curves in the absence or presence of an LRET acceptor. All experiments were repeated twice.

Optics photoluminescence and lanthanide signals overlap

Our studies of Eu³⁺–ATBTA-labeled beads revealed another limiting factor for lanthanide imaging. When using low bead-loading levels, we unexpectedly observed background signals that impeded lanthanide-probe imaging. We hypothesized that

this background photoluminescence originated from UV-light-excitable materials in the glass or in the optical coating of our microscope objective lenses. To investigate this possibility, we injected zebrafish zygotes with Eu^{3+}–DTBTA-functionalized 10-kDa dextran (30 fmol/embryo), which distributes uniformly among animal cells during development and is excluded from the yolk. We imaged the embryos at the 18-somite stage (16 hours postfertilization (hpf)), using two objectives with similar magnifications and numerical apertures (5×/0.15 NA and 6.3×/0.13 NA) but different 365-nm light transmission efficiencies (60% and 93%, respectively) (**Fig. 3a**). Steady-state imaging of the Eu^{3+}–DTBTA-injected embryos primarily captured yolk autofluorescence, and time-resolved imaging was able to selectively detect lanthanide luminescence and background instrument photoluminescence. The 6.3× objective with high UV-light transmittance yielded images with three- to five-fold-higher signal-to-background ratios than the UV-absorbing objective (**Fig. 3b**), thus implicating the lens materials in the observed background photoluminescence.

In contrast to autofluorescence, these optics-derived signals could not be selectively suppressed through time-gated emission acquisition or the addition of a narrow-band-pass filter (615/25 nm) (**Fig. 3b**). Optics photoluminescence is an inherent limitation of epifluorescence microscopy, because this imaging configuration uses the same objective lenses for sample illumination and detection. Time-resolved lanthanide microscopy is particularly sensitive to these long-lived background signals.

Lanthanide imaging with QSL transillumination

Our findings revealed how current lanthanide microscopy platforms are constrained by their reliance on LED illumination and epifluorescence configurations. We therefore developed a new modality for time-resolved lanthanide imaging that overcomes both limitations. First, we replaced the LED source with a 355-nm QSL. The QSL was able to deliver several microjoules of light energy to the sample within 15 ns, whereas a UV LED source typically delivers less than 1 μJ of light in a 1-μs pulse. We also devised a transreflected illumination configuration that prevents UV light from reaching the microscope objective, thereby averting UV-induced luminescence from the lenses (**Fig. 4a**). This configuration was accomplished by placing the sample on a TiO_2-coated coverglass that attenuated UV light by 100,000-fold but selectively transmitted longer-wavelength light with at least 90% efficiency (**Supplementary Fig. 6**).

To assess the efficacy of this system, we first examined its ability to minimize optics photoluminescence. We imaged Eu^{3+}–ATBTA-conjugated agarose beads by using four different objectives in the LED epi-illumination and QSL transreflected illumination configurations (**Fig. 4b**). We again used beads with minimal Eu^{3+}–ATBTA labeling, thus increasing the relative contribution of optics-derived background to the total luminescence. When the beads were imaged with LED epi-illumination and standard objectives, we observed signal-to-background ratios between 1.2 and 3.0. We were able to improve this ratio to 5.6 by using an objective with high UV-light transmittance. When we imaged the Eu^{3+}–ATBTA-conjugated beads by using QSL transillumination and the UV-light-reflecting coverglass, the signal-to-background ratios were up to 75-fold higher than those obtained with LED epi-illumination.

We then asked whether the new illumination method could enable efficient imaging of biological samples. For that purpose, we compared images acquired through steady-state fluorescence microscopy and through time-resolved photoluminescence microscopy (**Fig. 4c**). Fixed 16-hpf zebrafish embryos were stained with an anti–myosin heavy chain 1E (MYH1E) primary antibody and secondary antibodies labeled with commonly used fluorophores (Alexa Fluor 405, 488, and 594) or Eu^{3+}–DTBTA. Fluorescence microscopy captured not only Alexa Fluor signals from the labeled somites but
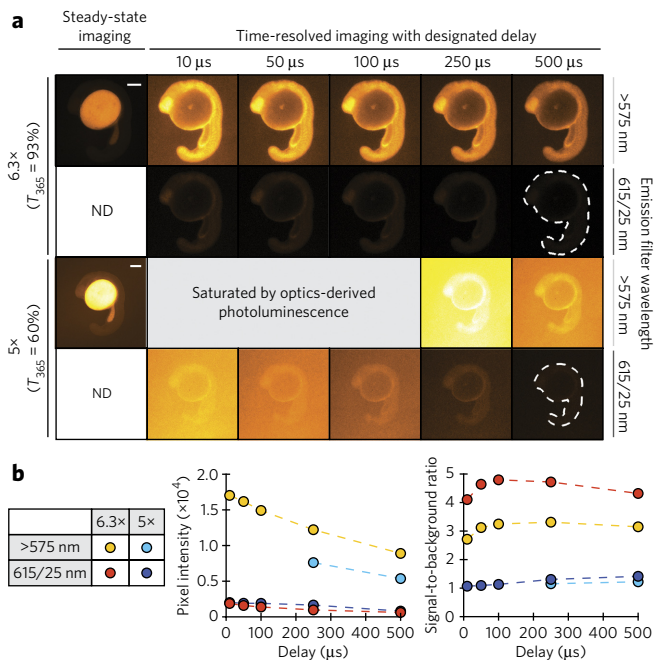

Figure 3 | Optics and lanthanide photoluminescence overlap temporally and spectrally. (**a**) Zebrafish embryos injected with Eu^{3+}–DTBTA-dextran (30 fmol/embryo) and then imaged by objectives with differing UV transmission efficiencies. Emission filters and time delays were also varied to assess the spectral and temporal properties of the optics-derived luminescence. Three zebrafish were analyzed per experimental condition, and representative micrographs of 16-hpf embryos are shown. Scale bar, 200 μm. T_{365}, 365-nm light transmission efficiency. (**b**) Left graph, average pixel intensities within the embryos (dashed outlines). Right graph, signal-to-background ratios of the time-resolved micrographs, with background defined as average pixel intensities outside the dashed outlines. ND, not determined. All experiments were repeated twice.

also yolk autofluorescence. In contrast, time-resolved microscopy using QSL transreflected illumination effectively minimized yolk autofluorescence and optics-derived background signals. As a result, the Eu^{3+}–DTBTA photoluminescence from the immunostained muscle cells was much more intense than the yolk-derived signals (**Fig. 4c**). By quantifying somite and yolk pixel intensities for each imaging configuration, we found that QSL transreflected imaging, compared with conventional epifluorescence microscopy, improved the signal-to-background ratio more than 25-fold.

We also compared the lanthanide-excitation rates that could be achieved with LED epi-illumination versus QSL transreflected illumination. We injected zebrafish zygotes with Eu^{3+}–DTBTA-functionalized 10-kDa dextran (**Fig. 5a**) and imaged the embryos at the 26-somite stage (22 hpf). The signal intensity from the injected dextran increased with LED pulse width in a manner consistent with the previously measured excitation and emission rates (**Fig. 2d**), thus allowing pixel intensities to be correlated with the fraction of excited lumiphores (**Fig. 5b**). A 1-ms LED illumination pulse excited approximately 20% of the lanthanide complexes, whereas a 10-μs pulse excited only 0.35%. By comparison, a 25.7-μJ QSL pulse excited 36% of the probe molecules in 15 ns. Using these signal intensities and the rate equations described in **Supplementary Figure 5**, we determined that the QSL k_{ex} values increased linearly with laser power, and the highest-energy pulse (25.7 μJ) achieved a k_{ex} value of 29.3×10^6 s^{-1}, representing an 81,900-fold increase over the LED excitation rate constant (**Supplementary Fig. 7**). These excitation rates far exceeded the k_{em} values for both intrinsic and LRET-enhanced lanthanide luminescence, and consequently excitation was
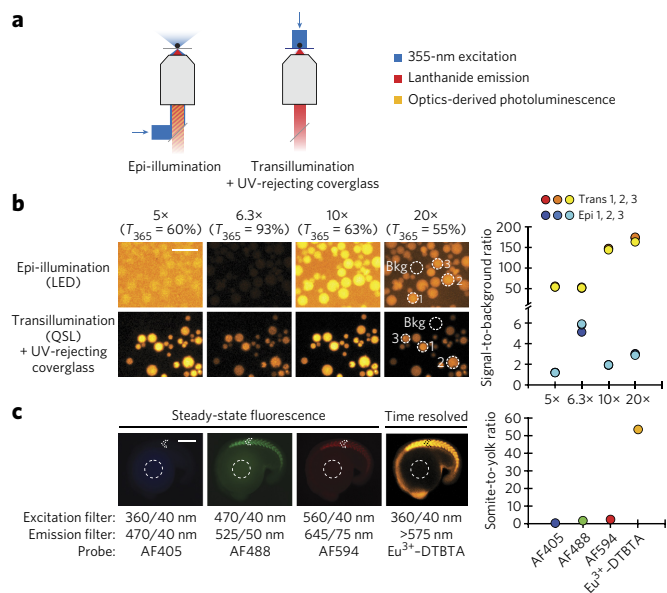
Figure 4 | QSL transreflected illumination overcomes optics-derived photoluminescence. (**a**) Optical paths of conventional epi-illumination (left) and transillumination (right) microscopy. The transillumination configuration also includes a UV-rejecting, TiO₂-coated coverglass placed between the sample and the objective. (**b**) Eu³⁺–ATBTA-functionalized beads imaged by time-resolved microscopy using the designated objectives and either LED epi-illumination (Epi) or QSL transreflected (Trans) illumination. Signal-to-background ratios for selected beads (dotted circles) are shown. Scale bar, 200 µm. Bkg, background. (**c**) Zebrafish embryos immunostained with an anti-MYH1E primary antibody and a secondary antibody conjugated with the designated probe. Steady-state fluorescence and time-resolved lanthanide luminescence micrographs of 16-hpf embryos and their corresponding somite-to-yolk pixel-intensity ratios are shown. Scale bar, 200 µm.

never rate limiting. Importantly, QSL transreflected illumination did not perturb zebrafish development and should therefore be compatible with live imaging (**Supplementary Fig. 8**). Optimized QSL imaging conditions, with 1-µJ pulses at 15 kHz, produced a time-averaged sample irradiance of 60 mW/cm² (Online Methods and **Supplementary Table 1**). This value was smaller than the 95 mW/cm² irradiance produced under optimized LED imaging conditions, which used 1-ms excitation pulses at 240 Hz.

Transreflected illumination with LRET (trLRET)

QSL transreflected illumination and LRET enhancement should synergistically improve the signal-to-background ratio and luminescence intensity in lanthanide imaging. We quantified this improvement by comparing trLRET with the conventional LED epi-illumination format (**Supplementary Fig. 9**). We used imaging protocols that were independently optimized for the two modalities, taking into account cycle rates, quantum yields, excited-state fractions, and decay rates (**Supplementary Fig. 10**). First, we imaged Eu³⁺–ATBTA beads, using 30 µM Atto 610 for the QSL trLRET condition (which decreased the luminescence lifetime of immobilized Eu³⁺–ATBTA to 14 µs; **Supplementary Fig. 10**). Because emission levels associated with the two methods differed by more than two orders of magnitude, we adjusted the camera gain to keep pixel intensities within a linear dynamic range (**Supplementary Fig. 11**). After normalizing for the differing gain values, we determined that the QSL trLRET signal intensities were 170-fold greater than those obtained with a pulsed LED and no LRET enhancement (**Supplementary Fig. 9**).
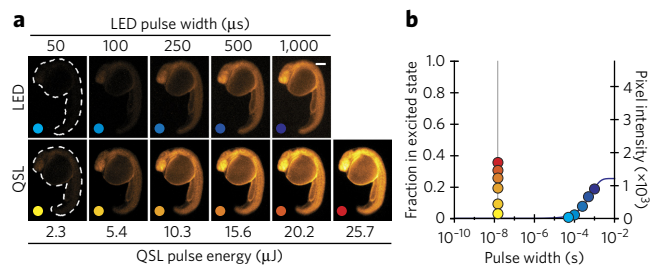

Figure 5 | QSL excitation dramatically increases lanthanide excitation rates. (**a**) Zebrafish embryos injected with Eu³⁺–DTBTA-dextran (60 fmol/embryo) and then imaged by time-resolved microscopy with a high-UV-transmittance objective and varying LED pulse widths or QSL pulse energies. At least three zebrafish were analyzed per experimental condition, and representative micrographs of 22-hpf embryos are shown. Scale bar, 200 µm. (**b**) Excited-state fractions and signal intensities of the lanthanide lumiphore for each illumination condition. The predicted excitation level is shown as a solid blue line ($R^2 = 0.985$). QSL illumination can achieve 20% excitation within 15 ns (vertical gray line), whereas LED illumination requires 1 ms. All experiments were repeated twice.

We then compared the performance of LED epifluorescence and QSL trLRET imaging in zebrafish. We immunostained 18-hpf embryos with the anti-MYH1E primary antibody and a mixture of labeled and unlabeled secondary antibodies. The labeled secondary antibodies were conjugated to either Alexa Fluor 594- or Eu³⁺–DTBTA (average labeling stoichiometry of 1.5 and 1.2 probes per antibody respectively; **Fig. 6a** and **Supplementary Fig. 12**). The total secondary-antibody concentration was fixed at 0.5 µg/mL to avoid any potential concentration-dependent changes in antibody affinity, and the labeled population was varied from 10% to 100%. Whole-mount immunostaining of zebrafish embryos and larvae typically uses fluorescently tagged secondary antibodies at concentrations of approximately 1–2 µg/mL. At lower antibody concentrations, the fluorescence signals were obscured by yolk and fixation-induced autofluorescence. Accordingly, we observed that 0.5 µg/mL Alexa Fluor 594-conjugated secondary antibody was required to visualize anti-MYH1E antibody-labeled somites by steady-state epifluorescence microscopy. When the embryos were imaged in the presence of 10 µM Atto 610 with the QSL trLRET system, the same primary antibody was readily detected at a ten-fold-lower concentration of Eu³⁺–DTBTA-conjugated secondary antibody (**Fig. 6a**).

Quantitative comparisons of the somite and yolk pixel intensities, which reflect specific immunostaining signals versus yolk autofluorescence and nonspecific antibody binding, confirmed that the new lanthanide imaging modality outperformed epifluorescence microscopy (**Fig. 6a**). Even at the lowest tested concentration of Eu³⁺–DTBTA-labeled secondary antibody, the somites in the trLRET images were 100-fold brighter than the yolk. Steady-state fluorescence images acquired with the same concentration of Alexa Fluor 594-conjugated secondary antibody had minimally detectable specific signals, with a somite-to-yolk ratio of 0.60. Together, our results illustrate how QSL trLRET can dramatically enhance the time-resolved imaging of lanthanide-based probes in whole organisms.

QSL trLRET imaging of molecular interactions *in vivo*

Like fluorescence resonance energy transfer, distance-dependent changes in intramolecular LRET efficiency can be used to detect molecular interactions or conformational states[20,22,36]. To explore this capability in the context of trLRET imaging, we tested whether we could visualize the binding of two macromolecules in live animals. We injected zebrafish zygotes with a Eu³⁺–DTBTA-labeled MO and either a complementary or noncomplementary MO labeled with Atto Rho14, an LRET acceptor that is stable *in vivo* (**Fig. 6b**).
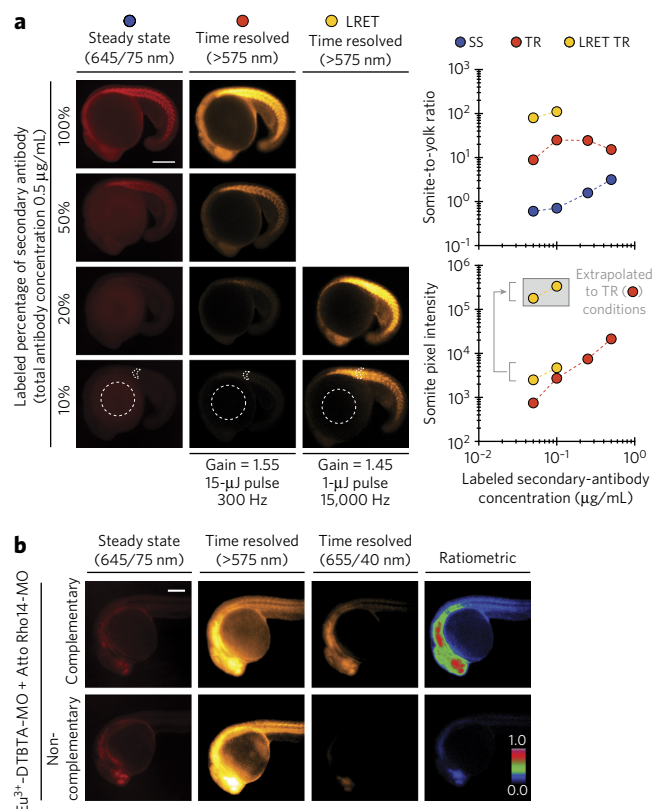
Figure 6 | trLRET enables ultrasensitive lanthanide imaging *in vivo*.
(**a**) Zebrafish embryos immunostained with a fixed concentration of anti-MYH1E primary antibody (15.3 μg/mL) and varying concentrations of AF594- or Eu^{3+}–DTBTA-conjugated secondary antibody. The Eu^{3+}–DTBTA-labeled embryos were imaged without or with LRET (30 μM Atto 610), with the designated camera gain, QSL pulse energy, cycle frequency, and emission filter. At least three zebrafish were analyzed per experimental condition, and representative micrographs of 18-hpf embryos and their corresponding somite-to-yolk pixel-intensity ratios and somite pixel intensities are shown. LRET pixel intensities normalized to the camera gain and QSL pulse energy used for non-LRET imaging are shown in the gray box. (**b**) Steady-state (SS) fluorescence and time-resolved (TR) luminescence micrographs of zebrafish embryos (24 hpf) injected at one-cell stage with a Eu^{3+}–DTBTA-labeled MO and either a complementary or noncomplementary MO labeled with Atto Rho14 (20 fmol of each MO per embryo; final *in vivo* concentrations of ~400 nM each). The emission filter used for each imaging modality is shown, and ratiometric micrographs were generated by normalizing LRET (time resolved, 655/40-nm) pixel intensities to those of steady-state Atto Rho14 fluorescence. The maximum ratiometric value was set to unity, thus resulting in mean values of 0.079 (complementary MOs) and 0.006 (noncomplementary MOs) for the micrographs. Three zebrafish were analyzed per experimental condition. Scale bars, 200 μm. All experiments were repeated twice.

We then imaged the embryos at 24 hpf, using the QSL trLRET system. These studies used a 575-nm long-pass filter to detect all emitted photons and a 655/40-nm filter to selectively detect LRET-induced Atto Rho14 fluorescence. Embryos injected with the complementary MOs exhibited 13-fold-higher LRET signal intensities than those injected with the noncomplementary oligonucleotides. Thus, trLRET microscopy can be used to visualize biochemically regulated interactions *in vivo*.

DISCUSSION

Time-resolved lanthanide imaging has lagged behind fluorescence microscopy, and its biological applications have been largely restricted to cultured cells and single-celled organisms[10,14,23,24,36].

Here, we demonstrated how QSL transreflected illumination and LRET-enhanced lanthanide decay can be used to overcome three key factors that have limited lanthanide imaging: low photon efflux, slow excitation rates, and optics-derived photoluminescence. These advances allowed us to establish a modality for time-resolved lanthanide imaging that can be readily applied to multicellular organisms, thus newly allowing the technology to surpass the detection limits of fluorescence microscopy.

The slow emission rates of photoluminescent lanthanide chelates intrinsically constrain imaging methods that capture direct lanthanide emissions. The signal-integration times required to compensate for low lanthanide photon flux are often impractical for biological applications and lead to higher levels of dark noise. Because biological and fixation-induced autofluorescence decays within tens of nanoseconds, probe lifetimes in the 0.1- to 10-μs regime arguably provide the best balance between total imaging time and background suppression. Luminescent complexes containing the transition metals Ir^{3+}, Re$^+$, Ru^{2+}, or Pt^{2+} have emission lifetimes that fall within this range; however, these reagents are highly oxygen sensitive; thus their versatility as biological probes is limited[37–40]. In comparison, lanthanide complexes are largely insensitive to chemical environment. As demonstrated by our studies, diffusion-mediated LRET is a simple and effective means for shortening lanthanide excited-state lifetimes to microsecond durations, thereby improving the performance of lanthanide probes in time-resolved imaging. Exploiting LRET to achieve 50-fold increases in lanthanide brightness is conceptually distinct from previous applications of LRET to sense changes in molecular structure[36,41,42].

The instrumentation commonly used for time-resolved lanthanide imaging also has intrinsic limitations. LEDs excite only a small fraction of lanthanide complexes with each illumination pulse, particularly when LRET enhancement is used to achieve microsecond-scale emission lifetimes. In addition, epi-illumination generates optics-derived photoluminescence that has lanthanide-like properties, thus limiting the signal-to-background improvements that can be achieved by autofluorescence suppression. QSL transreflected illumination addresses both of these issues. Because QSL photon flux is several thousand times greater than that of pulsed LEDs, a single QSL pulse can excite a substantial fraction of lanthanide-probe molecules, even when LRET enhancement is used. The transillumination configuration allows for placement of a UV-reflecting coverglass between the sample and microscope objective, thus preventing the excitation of photoluminescent materials in the lenses. In principle, optics-derived background signals could be averted by other approaches such as reflective objectives[43,44], dark-field microscopy[45], and light-sheet microscopy[46]. The planar illumination of light-sheet microscopy also suppresses sample autofluorescence and minimizes phototoxicity, and this method holds particular promise for time-resolved lanthanide imaging.

Using QSL transreflected illumination and time-resolved microscopy to image beads with minimal Eu^{3+}–ATBTA labeling, we observed signal-to-background ratios that were 75-fold higher than those obtained by LED epi-illumination. In addition, integrated signal intensities were 170-fold higher when QSL transreflected illumination was combined with diffusion-mediated LRET. These new capabilities are directly applicable to biological imaging, as illustrated by our studies of zebrafish embryos. We anticipate that trLRET will help establish lanthanide microscopy as a valuable tool for biological research, particularly for the detection of low-abundance proteins and transcripts in cells, tissues, or whole organisms. LRET-enhanced lanthanide imaging also has the potential for multiplexing, because individual lanthanide donor–acceptor pairs can be distinguished both spectrally and temporally[47,48]. Finally, lanthanide-based sensors have been used to visualize molecular interactions in cells[36], and our trLRET imaging system extends these capabilities to live organisms. Developing lanthanide chelates and probes with new functionalities will be important next steps toward realizing these capabilities.

METHODS

Methods, including statements of data availability and any associated accession codes and references, are available in the online version of the paper.

References

1. Grimm, J.B., Heckman, L.M. & Lavis, L.D. The chemistry of small-molecule fluorogenic probes. *Prog. Mol. Biol. Transl. Sci.* **113**, 1–34 (2013).
2. Rodriguez, E.A. *et al.* The growing and glowing toolbox of fluorescent and photoactive proteins. *Trends Biochem. Sci.* **42**, 111–129 (2017).
3. Shu, X. *et al.* Mammalian expression of infrared fluorescent proteins engineered from a bacterial phytochrome. *Science* **324**, 804–807 (2009).
4. Shcherbakova, D.M. & Verkhusha, V.V. Near-infrared fluorescent proteins for multicolor *in vivo* imaging. *Nat. Methods* **10**, 751–754 (2013).
5. Bertrand, E. *et al.* Localization of ASH1 mRNA particles in living yeast. *Mol. Cell* **2**, 437–445 (1998).
6. Raj, A., van den Bogaard, P., Rifkin, S.A., van Oudenaarden, A. & Tyagi, S. Imaging individual mRNA molecules using multiple singly labeled probes. *Nat. Methods* **5**, 877–879 (2008).
7. Choi, H.M.T. *et al.* Programmable *in situ* amplification for multiplexed imaging of mRNA expression. *Nat. Biotechnol.* **28**, 1208–1212 (2010).
8. Tanenbaum, M.E., Gilbert, L.A., Qi, L.S., Weissman, J.S. & Vale, R.D. A protein-tagging system for signal amplification in gene expression and fluorescence imaging. *Cell* **159**, 635–646 (2014).
9. Connally, R.E. & Piper, J.A. Time-gated luminescence microscopy. *Ann. NY Acad. Sci.* **1130**, 106–116 (2008).
10. Jin, D. *et al.* How to build a time-gated luminescence microscope. *Curr. Protoc. Cytom.* **67**, 2.22 (2014).
11. Beverloo, H.B., van Schadewijk, A., van Gelderen-Boele, S. & Tanke, H.J. Inorganic phosphors as new luminescent labels for immunocytochemistry and time-resolved microscopy. *Cytometry* **11**, 784–792 (1990).
12. Marriott, G., Clegg, R.M., Arndt-Jovin, D.J. & Jovin, T.M. Time resolved imaging microscopy: phosphorescence and delayed fluorescence imaging. *Biophys. J.* **60**, 1374–1387 (1991).
13. Seveus, L. *et al.* Time-resolved fluorescence imaging of europium chelate label in immunohistochemistry and in situ hybridization. *Cytometry* **13**, 329–338 (1992).
14. Marriott, G., Heidecker, M., Diamandis, E.P. & Yan-Marriott, Y. Time-resolved delayed luminescence image microscopy using an europium ion chelate complex. *Biophys. J.* **67**, 957–965 (1994).
15. Moore, E.G., Jocher, C.J., Xu, J., Werner, E.J. & Raymond, K.N. An octadentate luminescent Eu(III) 1,2-HOPO chelate with potent aqueous stability. *Inorg. Chem.* **46**, 5468–5470 (2007).
16. Montgomery, C.P., Murray, B.S., New, E.J., Pal, R. & Parker, D. Cell-penetrating metal complex optical probes: targeted and responsive systems based on lanthanide luminescence. *Acc. Chem. Res.* **42**, 925–937 (2009).
17. Bünzli, J.-C.G. Lanthanide luminescence for biomedical analyses and imaging. *Chem. Rev.* **110**, 2729–2755 (2010).
18. Xu, J. *et al.* Octadentate cages of Tb(III) 2-hydroxyisophthalamides: a new standard for luminescent lanthanide labels. *J. Am. Chem. Soc.* **133**, 19900–19910 (2011).
19. Heffern, M.C., Matosziuk, L.M. & Meade, T.J. Lanthanide probes for bioresponsive imaging. *Chem. Rev.* **114**, 4496–4539 (2014).
20. Dickson, E.F., Pollak, A. & Diamandis, E.P. Ultrasensitive bioanalytical assays using time-resolved fluorescence detection. *Pharmacol. Ther.* **66**, 207–235 (1995).
21. Hagan, A.K. & Zuchner, T. Lanthanide-based time-resolved luminescence immunoassays. *Anal. Bioanal. Chem.* **400**, 2847–2864 (2011).
22. Emami-Nemini, A. *et al.* Time-resolved fluorescence ligand binding for G protein-coupled receptors. *Nat. Protoc.* **8**, 1307–1320 (2013).
23. Connally, R., Jin, D. & Piper, J. High intensity solid-state UV source for time-gated luminescence microscopy. *Cytometry A* **69**, 1020–1027 (2006).
24. Gahlaut, N. & Miller, L.W. Time-resolved microscopy for imaging lanthanide luminescence in living cells. *Cytometry A* **77**, 1113–1125 (2010).
25. Rajendran, M. & Miller, L.W. Evaluating the performance of time-gated live-cell microscopy with lanthanide probes. *Biophys. J.* **109**, 240–248 (2015).
26. Moore, E.G., Samuel, A.P. & Raymond, K.N. From antenna to assay: lessons learned in lanthanide luminescence. *Acc. Chem. Res.* **42**, 542–552 (2009).
27. Bünzli, J.C. & Piguet, C. Taking advantage of luminescent lanthanide ions. *Chem. Soc. Rev.* **34**, 1048–1077 (2005).
28. Armelao, L. *et al.* Design of luminescent lanthanide complexes: from molecules to highly efficient photo-emitting materials. *Coord. Chem. Rev.* **254**, 487–505 (2010).
29. Mathis, G. & Bazin, H. in *Lanthanide Luminescence* 47–88 (Springer, 2011).
30. Byegård, J., Skarnemark, G. & Skålberg, M. The stability of some metal edta, dtpa and dota complexes: application as tracers in groundwater studies. *J. Radioanal. Nucl. Chem.* **241**, 281–290 (1999).
31. Firsching, F.H. & Brune, S.N. Solubility products of the trivalent rare-earth phosphates. *J. Chem. Eng. Data* **36**, 93–95 (1991).
32. Chen, J. & Selvin, P.R. Synthesis of 7-amino-4-trifluoromethyl-2-(1H)-quinolinone and its use as an antenna molecule for luminescent europium polyaminocarboxylates chelates. *J. Photochem. Photobiol. Chem.* **135**, 27–32 (2000).
33. Nishioka, T. *et al.* New luminescent europium(III) chelates for DNA labeling. *Inorg. Chem.* **45**, 4088–4096 (2006).
34. Hanaoka, K., Kikuchi, K., Kobayashi, S. & Nagano, T. Time-resolved long-lived luminescence imaging method employing luminescent lanthanide probes with a new microscopy system. *J. Am. Chem. Soc.* **129**, 13502–13509 (2007).
35. Thomas, D.D., Carlsen, W.F. & Stryer, L. Fluorescence energy transfer in the rapid-diffusion limit. *Proc. Natl. Acad. Sci. USA* **75**, 5746–5750 (1978).
36. Rajapakse, H.E. *et al.* Time-resolved luminescence resonance energy transfer imaging of protein-protein interactions in living cells. *Proc. Natl. Acad. Sci. USA* **107**, 13582–13587 (2010).
37. Yam, V.W. & Wong, K.M. Luminescent metal complexes of d6, d8 and d10 transition metal centres. *Chem. Commun. (Camb.)* **47**, 11579–11592 (2011).
38. Thorp-Greenwood, F.L., Balasingham, R.G. & Coogan, M.P. Organometallic complexes of transition metals in luminescent cell imaging applications. *J. Organomet. Chem.* **714**, 12–21 (2012).
39. Botchway, S.W. *et al.* Time-resolved and two-photon emission imaging microscopy of live cells with inert platinum complexes. *Proc. Natl. Acad. Sci. USA* **105**, 16071–16076 (2008).
40. de Haas, R.R. *et al.* Phosphorescent platinum/palladium coproporphyrins for time-resolved luminescence microscopy. *J. Histochem. Cytochem.* **47**, 183–196 (1999).
41. Selvin, P.R. Lanthanide-based resonance energy transfer. *IEEE J. Sel. Top. Quantum Electron.* **2**, 1077–1087 (1996).
42. Kubota, T. *et al.* Mapping of voltage sensor positions in resting and inactivated mammalian sodium channels by LRET. *Proc. Natl. Acad. Sci. USA* **114**, E1857–E1865 (2017).
43. Norris, K.P., Seeds, W.E. & Wilkins, M.H.F. Reflecting microscopes with spherical mirrors. *J. Opt. Soc. Am.* **41**, 111–119 (1951).
44. Miyata, S., Yanagawa, S. & Noma, M. Reflecting microscope objectives with nonspherical mirrors. *J. Opt. Soc. Am.* **42**, 431–432 (1952).
45. Witlin, B. Darkfield illuminators in microscopy. *Science* **102**, 41–42 (1945).
46. Huisken, J., Swoger, J., Del Bene, F., Wittbrodt, J. & Stelzer, E.H. Optical sectioning deep inside live embryos by selective plane illumination microscopy. *Science* **305**, 1007–1009 (2004).
47. Lu, Y. *et al.* Tunable lifetime multiplexing using luminescent nanocrystals. *Nat. Photonics* **8**, 32–36 (2014).
48. Chen, J.Y. & Selvin, P.R. Lifetime- and color-tailored fluorophores in the micro- to millisecond time regime. *J. Am. Chem. Soc.* **122**, 657–660 (2000).

Author contributions

K.S.K. and J.K.C. built the time-resolved LED epifluorescence microscope; P.B.H. conceived the LRET-enhanced imaging by tuning lanthanide-lumiphore lifetimes; U.C. and P.B.H. conceived, designed, and built the QSL transreflected-illumination system; U.C., D.P.R., P.C., K.S.K., J.K.C., and P.B.H. designed the experiments; U.C. and P.C. performed the imaging experiments; U.C., D.P.R., P.C., K.S.K., J.K.C., and P.B.H. analyzed data; U.C., J.K.C., and P.B.H. wrote the paper.

Competing financial interests

The authors declare no competing financial interests.

Additional information

Any supplementary information, chemical compound information and source data are available in the online version of the paper. Reprints and permissions information is available online at http://www.nature.com/reprints/index.html. Publisher's note: Springer Nature remains neutral with regard to jurisdictional claims in published maps and institutional affiliations. Correspondence and requests for materials should be addressed to J.K.C. or P.B.H.

ONLINE METHODS

Time-resolved luminescence and steady-state microscopy. Time-resolved imaging was conducted with a Leica DMI6000B inverted microscope, a Stanford Photonics XR/MEGA-10Z ICCD camera, a Prizmatix 365-nm LED (Mic-LED-365), a Spectra-Physics 355-nm QSL (Explorer One 355-300), and a Quantum Composers four-channel pulse generator (model 9514). Communication between the QSL and four-channel pulse generator was mediated by a breakout board (Winford Engineering; BRKSD26HDF-R), a wire lead-to-BNC male cable (Pomona Electronics; 4970), and a BNC female-to-BNC male cable (AV-Cables.net). The integrated system was controlled with Piper Software (ICCD camera; version 2.6.84) and L-Win software (QSL; version 1.5.11), with the image-acquisition parameters shown in **Supplementary Table 2**. Steady-state fluorescence imaging was conducted with a Photometric CoolSNAP HQ CCD camera, a Leica EL6000 external light source, and MetaMorph software (version 7.8), with the exception of the data set for **Supplementary Figure 8**. For those micrographs, a Leica DM4500B upright compound microscope equipped with a 5×/0.12-NA Plan objective and a Retiga-SRV Fast 1394 camera were used. Images were acquired with the following objectives: HCX PL S-APO 5×/0.15 NA, HCX PL FLUOTAR UVI 6.3×/0.13 NA, HCX PL FLUOTAR 10×/0.30 NA, and HCX PL FLUOTAR L 20×/0.40 NA. Filter sets used in these studies were: DAPI (excitation, 360/40 nm; emission, 470/40 nm), GFP (excitation, 470/40 nm; emission, 525/50 nm), TX2 (excitation, 560/40 nm; emission, 645/75 nm), and lanthanide (excitation, 360/40 nm; emission, >575 nm). Further details about the LED and QSL illumination methods are provided in **Supplementary Table 1**. The QSL transillumination setup is depicted in **Supplementary Figure 13**. Briefly, a cage system was built around the microscope body by using UV-enhanced aluminum mirrors (Thorlabs; PF10-03-F01) to direct the QSL beam to the stage. This transillumination light path projected a 4-mm illuminated disc with an area of 0.126 cm² onto the sample. Light pulses of 1 μJ at 15,000 Hz were typically used for QSL trLRET imaging. After the 50% transmission efficiency from laser to stage was accounted for, this power corresponded to 7,500 μJ/s or equivalently 7.5 mW. The time-averaged irradiance at the sample was therefore 7.5/0.126 = 60 mW/cm².

TiO₂-coated coverslips for trLRET imaging. The following coverslips were coated with TiO₂ at IOS Optics: 0.25- and 0.50-mm thick, 25.4-mm-diameter sapphire (Ted Pella; 16005-1010 and 16005-1020); 0.2-mm thick, 25.4-mm-diameter fused quartz (Technical Glass Products); and no. 1.5, 25.4-mm diameter borosilicate glass (Warner Instruments; 64-0715). No thermal damage or mechanical warping was observed during the coating process. An overlying protective SiO₂ layer was also added. Under QSL illumination, the sapphire and fused quartz coverslips did not generate any detectable background, whereas some long-lived photoluminescence was observed from the coated borosilicate coverslips. All experiments were performed with the sapphire coverslips because of ease of handling and the absence of background emission.

Zebrafish-embryo injections and imaging. All zebrafish experiments were conducted with wild-type AB fish (Zebrafish International Resource Center), in compliance with protocol 10511 approved by the Stanford University Institutional Animal Care and Use Committee. Embryos were obtained by natural mating and cultured in E3 medium at 28 °C. All embryo injections (typically 1–2 nL/embryo) were conducted in E3 medium at room temperature. For live-imaging studies, the embryos were manually dechorionated and then immobilized in E3 medium containing 1.5% (w/v) low-melting-point agarose. Animal studies were conducted without blinding.

Preparation of Eu³⁺–ATBTA-functionalized beads. Eu³⁺–ATBTA (TCI) was dissolved in 20 mM HEPES buffer, pH 8, to prepare a 1 mM solution of the lanthanide complex. N-hydroxysuccinimide (NHS) ester–activated agarose beads (1 mg; Thermo Scientific) were shaken in 0.5 mL of the 1 mM Eu³⁺–ATBTA solution at room temperature for either 1 min or 16 h, depending on the desired degree of Eu³⁺–ATBTA loading. Low loading levels were used to determine lanthanide excitation rates and to establish methods for minimizing optics-derived photoluminescence and maximizing lanthanide detection sensitivity. The reaction was then centrifuged to remove supernatant, and the beads were washed with 20 mM HEPES buffer, pH 8 (3 × 0.5 mL), before use.

Homogeneous-solution assays. Lanthanide luminescence in homogeneous solutions was measured with a Tecan Infinite M1000 Pro microtiter plate reader, with the instrument configurations described in **Supplementary Table 3**. Sulfo-Cy3 and sulfo-Cy5 reagents were purchased from Lumiprobe; Atto 610 and sodium ascorbate were purchased from Sigma-Aldrich; and dNTPs were purchased from Life Technologies. To determine the lifetimes of LRET-mediated lanthanide luminescence, signal intensities were measured for a series of 'time slices.' Collection times were fixed at 100 μs, and the temporal delay was varied from 0 to 400 μs. The integrated signal intensities of these time slices were fitted to the equation below in MATLAB software (version R2015b).

$$y(t) = c \times \int_{\text{delay}}^{\text{delay} + 100} e^{-t/\tau} dt$$

To compare the integrated signal intensities of Eu³⁺–ATBTA complexes in the absence and presence of 10 μM Atto 610 (i.e., integrated emission spectra from 0 μs after excitation to infinity), emission photons were collected for 2 ms (the maximum collection time permitted by the instrument) after a delay of 30 μs. The measured signal intensities for this pulse cycle and average luminescence lifetimes (1,020 and 17 μs in the absence and presence of Atto 610, respectively) were then used to calculate total photon emissions for each experimental condition.

Determination of the Eu³⁺–ATBTA quantum yield (QY_{Eu}). LRET emission is $(E_{\text{LRET}} \times QY_{\text{acceptor}})/QY_{\text{Eu}}$ times brighter than direct Eu³⁺ emission (**Fig. 1a**). In the presence of 10 μM Atto 610, we observed that LRET emission was 1.8-fold more efficient than the direct Eu³⁺ emission for the Eu³⁺–ATBTA complex, as determined by comparing their integrated spectra (**Fig. 1d**). Because the E_{LRET} under these conditions was 98% $(1 - \tau_{+\text{LRET}}/\tau_{-\text{LRET}})$, and the quantum yield of Atto 610 has been reported to be 70%, we estimated the Eu³⁺–ATBTA quantum yield to be 38%.

Diffusion-enhanced LRET curve fitting. LRET-enhanced lanthanide luminescence was modeled with equations (1) and (2), as previously described[35]:

$$E_{\text{LRET}} = \frac{k_r}{k_0 + k_r} = 1 - \frac{\tau}{\tau_0} \tag{1}$$

where E_{LRET} is the LRET efficiency, τ is the lanthanide-complex lifetime in the presence of an acceptor, τ_0 is the lanthanide-complex lifetime in the absence of an acceptor, k_0 is the rate constant for lanthanide emission in the absence of an acceptor = $1/\tau_0$, and k_r is the rate constant for the energy transfer, and

$$k_r = \frac{4\pi\rho R_0^6}{3\tau_0 a^3} \tag{2}$$

where ρ is the density of acceptor molecules (concentration), R_0 is the distance between the donor and acceptor at which the LRET efficiency is 50%, and a is the distance of closest approach between the donor and acceptor.

Equation (2) can be simplified as $k_r = c \times \rho/\tau_0$, where c is a constant for a given LRET pair. Using this abridged description of k_r and defining $k_0 = 1/\tau_0$, Eq. (1) can be rewritten as equation (3). Equation (3) can be further simplified to equation (4), which shows the relationship between the acceptor concentration (ρ) and LRET lifetime (τ):

$$\frac{\dfrac{c\rho}{\tau_0}}{\dfrac{1}{\tau_0} + \dfrac{c\rho}{\tau_0}} = 1 - \frac{\tau}{\tau_0} \tag{3}$$

$$\tau = \tau_0\left(\frac{1}{1 + c\rho}\right) \tag{4}$$

Synthesis of cs124-CF₃ (7-amino-4-trifluoromethyl-2(1H)-quinolinone). cs124-CF₃ was prepared according to a previously reported procedure[48]. 1,3-phenylenediamine (100 mg, 0.925 mmol), zinc chloride (139 mg, 1.02 mmol), and ethyl 4,4,4-trifluoroacetoacetate (187 mg, 0.925 mmol) were dissolved in 1 mL DMSO. The reaction mixture was stirred at 150 °C for 48 h. After being cooled to room temperature, the reaction was added to 10 mL water

and extracted with diethyl ether (3 × 20 mL). The organic layers were combined, dried over anhydrous $MgSO_4$, and concentrated under reduced pressure. The crude product was purified by silica-gel chromatography and elution with hexane/EtOAc (from 4:1 to 1:4), thus affording a beige powder (47.6 mg, 22.6%). ^{1}H NMR (400 MHz, CD_3OD) δ = 6.53 (s, 1H), 6.55 (s, 1H), 6.68 (d, J = 7.2 Hz, 1H), 7.50 (d, J = 7.2 Hz, 1H) (**Supplementary Fig. 14**). HRMS–ESI (m/z): [M + H]$^+$ calculated for $C_{10}H_8O_1N_2F_3$, 229.0583; observed, 229.0590.

Synthesis of DTPA–cs124-CF$_3$ (diethylenetriaminepentaacetic acid–7-amino -4-trifluoro-methyl-2(1H)-quinolinone). DTPA–cs124-CF$_3$ was prepared according to a previously reported procedure[20]. Diethylenetriaminepentaacetic acid (DTPA) dianhydride (17.2 mg, 0.0481 mmol) and triethylamine (58.0 mg, 0.573 mmol) were dissolved in 1.1 mL DMF. To this solution, cs124-CF$_3$ (9.0 mg, 0.039 mmol) in 0.5 mL DMF was added dropwise. After being stirred at room temperature for 1 h, the reaction was quenched with 3.5 mL of 1 M triethylammonium acetate, pH 6.5. The reaction product was then purified by HPLC. Yield: 10.0 mg (42.5%). ^{1}H NMR (400 MHz, CD_3OD) δ = 3.25 (m, 4H), 3.55 (m, 4H), 3.65 (m, 6H), 3.75 (s, 2H), 4.45 (s, 2H), 6.88 (s, 1H), 7.40 (d, J = 8.5 Hz, 1H), 7.76 (d, J = 8.5 Hz, 1H), 8.18 (s, 1H) (**Supplementary Fig. 15**). HRMS–ESI (m/z): [M + H]$^+$ calculated for $C_{24}H_{29}O_{10}N_5F_3$, 604.1861; observed, 604.1849.

Synthesis of Eu^{3+}–DTBTA (cyanuric chloride–activated Eu^{3+}–ATBTA). Eu^{3+}–ATBTA (1.2 mg, 1.4 µmol) was dissolved in ice-cold 0.1 M acetate buffer (pH 5; 60 µL). To this solution was added cyanuric chloride (0.70 mg, 3.8 µmol; Aldrich) in ice-cold acetone (25 µL). After the reaction mixture was incubated at 10 °C for 120 min, acetone (1 mL) was added dropwise. The resulting precipitate was pelleted by centrifugation at 17,000g for 1 min, washed with acetone (2 × 0.5 mL), and dried *in vacuo* to obtain Eu^{3+}–DTBTA as a yellow powder (80–90% yield). The full conversion of Eu^{3+}–ATBTA to Eu^{3+}–DTBTA was confirmed by LC/MS analysis. HRMS–ESI (m/z): [M – H]$^-$ calculated for $C_{40}H_{30}O_8N_9Cl_2Eu$, 986.0734; observed, 986.0714. The Eu^{3+}–DTBTA was then stored as a 1.5 mM aqueous solution at −20 °C.

Preparation of labeled secondary antibodies. Goat anti-mouse IgG (100 µL, Jackson ImmunoResearch; 115-005-146 (**Fig. 4c**) or Thermo Fisher Scientific; 31160 (**Fig. 6a** and **Supplementary Fig. 12**)) was dialyzed against conjugation buffer (150 mM NaCl and 10 mM HEPES, pH 8) at room temperature and 4 °C (3 × 300 mL; 2 h, 2 h, and overnight), with a 10-kDa molecular-weight-cutoff dialysis cup (Thermo Scientific). An ~1 mM solution of Eu^{3+}–DTBTA or Alexa Fluor 594 NHS ester (Thermo Fisher Scientific; A20004) in ice-cold conjugation buffer was prepared immediately before use, and 5 µL of this solution was added to 100 µL of the dialyzed antibody solution. After the reaction mixture was incubated at room temperature overnight, unreacted Eu^{3+}–DTBTA was removed by two rounds of size-exclusion chromatography (Illustra MicroSpin G-50; GE Healthcare Life Sciences). The resulting stock solution of Eu^{3+}–DTBTA-labeled and Alexa Fluor 594–labeled secondary antibody exhibited red fluorescence under 365-nm illumination. The probe-to-antibody ratios were calculated from absorbance levels at 341 nm (Eu^{3+}–DTBTA), 594 nm (Alexa Fluor 594), and 280 nm (antibody), as determined with a NanoDrop spectrophotometer (Thermo Scientific).

Preparation of labeled MOs. *Eu^{3+}–DTBTA-labeled MOs.* A nontargeting control MO (5′-GACAACCACTACCTGAGCACCCAGT-3′; Gene Tools) with a 3′ primary amine (6 nmol) was incubated with Eu^{3+}–DTBTA (56 nmol) in 0.2 M HEPES (100 µL, pH 8) buffer, and the reaction mixture was shaken at room temperature overnight in the dark. Excess Eu^{3+}–DTBTA was removed by size-exclusion chromatography (NAP-5 column (GE Healthcare Life Sciences) and/or a Sep-Pak C18 1-cc Vac cartridge (Waters)) to obtain the Eu^{3+}–DTBTA-labeled MOs. MS–ESI: m/z calculated for $C_{336}H_{496}O_{105}N_{158}P_{25}Cl_1Eu_1$ [M + H]$^+$: 9,390; observed: 9,390.

Atto Rho14-labeled MOs. An MO (5′–ACTGGGTGCTCAGGTAGTGG TTGTC–3′ or 5′–GCTGTTGTAGTTGTACTCCAGCTTG–3′) with a 5′ primary amine (6 nmol) was incubated with Atto Rho14 NHS ester (41 nmol; Sigma) in 0.2 M HEPES buffer (70 µL, pH 8) and DMSO (10 µL), and the reaction mixture was shaken at room temperature for 4 h in the dark. Excess Atto Rho14 NHS ester was removed by size-exclusion chromatography. MS–ESI (m/z): (1) [M + H]$^+$ calculated for $C_{312}H_{487}O_{109}N_{151}P_{25}$ + 766.6 (Atto Rho14), 9,638; observed, 9,638 and (2) [M + H]$^+$ calculated for $C_{311}H_{489}O_{111}N_{143}P_{25}$ + 766.6 (Atto Rho14), 9,548; observed, 9,548.

Preparation of Eu^{3+}–DTBTA-labeled dextran. 10-kDa dextran amine (1 nmol; Molecular Probes) in 7.5 µL conjugation buffer (150 mM NaCl and 10 mM HEPES, pH 8) was added to a 1.2 mM solution of Eu^{3+}–DTBTA (7.5 µL) in the same buffer. The reaction mixture was incubated at room temperature for 3 h in the dark. Excess Eu^{3+}–DTBTA was then removed by size-exclusion chromatography (Illustra MicroSpin G-50; GE Healthcare Life Sciences).

Immunostaining of zebrafish embryos. Primary and secondary antibodies used for the various experiments are shown in **Supplementary Table 4**. Wild-type AB zebrafish embryos at the desired developmental stage were dechorionated in E3 medium and fixed in freshly prepared 4% paraformaldehyde in PBS for 90 min at room temperature. After fixation, the embryos were washed with PBS containing 0.5% (v/v) Triton X-100 (4 × 1 mL; 10 min per wash) and treated for 90 min at room temperature with a 1-mL aqueous solution of 10 mM Tris-HCl, pH 7.5, 250 mM NaCl, 10% (v/v) sheep serum, 0.5% (v/v) Triton X-100, and 0.5% (w/v) bovine serum albumin. After the blocking solution was removed, the embryos were incubated with anti-MYH1E antibody (1:15 dilution, Developmental Studies Hybridoma Bank, MF20) at 4 °C overnight in 500 µL blocking solution. The primary-antibody solution was then removed, and the embryos were washed with a 1-mL solution of 10 mM Tris-HCl, pH 7.5, 250 mM NaCl, and 0.5% (v/v) Triton X-100 (TBSX) (4 × 5 min and then 3 × 20 min). After 90 min of additional blocking, the embryos were incubated with varying dilutions of preadsorbed Alexa Fluor– or Eu^{3+}–DTBTA-labeled secondary antibody in 500 µL blocking solution for 1.5 h at room temperature. (The secondary antibodies were preadsorbed against 20–30 fixed zebrafish embryos as a 1:500 dilution in 1 mL blocking solution for 1.5 h at room temperature.) The samples were subsequently washed with 1 mL TBSX (5 × 5 min and then 3 × 20 min) and mounted in an aqueous solution containing 1.5% (w/v) low-melting-point agarose. For trLRET imaging, embryos were incubated in TBSX supplemented with 30 µM Atto 610 for 15 min, and then mounted in low-melting-point agarose containing the same concentration of Atto 610.

Image and statistical analyses. Quantitative analyses of bead micrographs used at least three beads per imaging condition, with each bead corresponding to several thousand pixels. For zebrafish imaging experiments, embryos were obtained from at least two breeding tanks, each containing two to four males and two to four females from separate adult stocks. The embryos were collected within the first 15 min of natural mating, pooled, and then randomly distributed. No blinding was applied. Quantitative analyses of zebrafish micrographs used at least three embryos per imaging condition, with each embryo corresponding to several hundred thousand pixels. Background levels were based on adjacent regions composed of several thousand pixels. To determine somite-to-yolk ratios, image analyses used circumscribed regions within somitic (several thousand pixels) or yolk (tens of thousands of pixels) tissues. The P value in **Supplementary Figure 9c** was calculated with a two-tailed t test assuming equal variance.

Data availability. The data that support the findings of this study are available from the corresponding authors on reasonable request. A **Life Sciences Reporting Summary** for this paper is available.

nature research

Corresponding author(s): James K. Chen and Pehr B. Harbury

☐ Initial submission   ☐ Revised version   ☒ Final submission

Life Sciences Reporting Summary

Nature Research wishes to improve the reproducibility of the work that we publish. This form is intended for publication with all accepted life science papers and provides structure for consistency and transparency in reporting. Every life science submission will use this form; some list items might not apply to an individual manuscript, but all fields must be completed for clarity.

For further information on the points included in this form, see Reporting Life Sciences Research. For further information on Nature Research policies, including our data availability policy, see Authors & Referees and the Editorial Policy Checklist.

▶ Experimental design

1. **Sample size**

   Describe how sample size was determined.

   We analyzed multiple beads (3-5) for each experimental condition shown in Fig. 2a, Fig. 2d, Fig. 4b, Supplementary Fig. 9c, and Supplementary Fig. 10a. Each bead within a micrograph is composed of several thousand pixels, which were used to calculate average pixel intensities.

   At least 3 zebrafish embryos were analyzed per each experimental condition. Representative micrographs are shown in Fig. 3a, Fig. 4c, Fig. 5a, Fig. 6, Supplementary Fig. 3, Supplementary Fig. 8c, and Supplementary Fig. 12. Each embryo within a micrograph is composed of several hundred thousand pixels, which were used to calculate average pixel intensities. Background levels were based on adjacent regions composed of several thousand pixels. To determine somite-to-yolk ratios, image analyses utilized circumscribed regions within somitic (several thousand pixels) or yolk (tens of thousands of pixels) tissues.

2. **Data exclusions**

   Describe any data exclusions.

   Unfertilized and developmentally abnormal embryos (typically 10-20% of the total clutch) were removed prior to imaging.

3. **Replication**

   Describe whether the experimental findings were reliably reproduced.

   All experimental findings were reliably reproduced.

4. **Randomization**

   Describe how samples/organisms/participants were allocated into experimental groups.

   We utilized the following protocol for the zebrafish studies shown in Fig. 3a, Fig. 4c, Fig. 5a, Fig. 6, Supplementary Fig. 3, Supplementary Fig. 8c, and Supplementary Fig. 12. Zebrafish embryos were obtained from at least two breeding tanks, each containing 2-4 males and 2-4 females from separate adult stocks. The embryos were collected within the first 15 minutes of natural mating, pooled, and then randomly distributed

5. **Blinding**

   Describe whether the investigators were blinded to group allocation during data collection and/or analysis.

   Not applicable

Note: all studies involving animals and/or human research participants must disclose whether blinding and randomization were used.

6. Statistical parameters

For all figures and tables that use statistical methods, confirm that the following items are present in relevant figure legends (or in the Methods section if additional space is needed).

n/a	Confirmed	
☐	☒	The <u>exact sample size</u> (*n*) for each experimental group/condition, given as a discrete number and unit of measurement (animals, litters, cultures, etc.)
☐	☒	A description of how samples were collected, noting whether measurements were taken from distinct samples or whether the same sample was measured repeatedly
☐	☒	A statement indicating how many times each experiment was replicated
☐	☒	The statistical test(s) used and whether they are one- or two-sided (note: only common tests should be described solely by name; more complex techniques should be described in the Methods section)
☐	☒	A description of any assumptions or corrections, such as an adjustment for multiple comparisons
☐	☒	The test results (e.g. *P* values) given as exact values whenever possible and with confidence intervals noted
☐	☒	A clear description of statistics including <u>central tendency</u> (e.g. median, mean) and <u>variation</u> (e.g. standard deviation, interquartile range)
☐	☒	Clearly defined error bars

See the web collection on statistics for biologists for further resources and guidance.

▶ Software

Policy information about availability of computer code

7. Software

Describe the software used to analyze the data in this study.

> MATLAB (version R2015b) and KaleidaGraph (version 4.1.3) software

For manuscripts utilizing custom algorithms or software that are central to the paper but not yet described in the published literature, software must be made available to editors and reviewers upon request. We strongly encourage code deposition in a community repository (e.g. GitHub). *Nature Methods* guidance for providing algorithms and software for publication provides further information on this topic.

▶ Materials and reagents

Policy information about availability of materials

8. Materials availability

Indicate whether there are restrictions on availability of unique materials or if these materials are only available for distribution by a for-profit company.

> No unique materials were used

9. Antibodies

Describe the antibodies used and how they were validated for use in the system under study (i.e. assay and species).

> The anti-MYH1E antibody was initially validated by Bader et al. J. Cell. Biol. 95:763-70 (1982), and it has been reported in over 200 zebrafish studies to date (www.zfin.org). Secondary antibodies were validated by the manufacturers. The antibodies used in our studies are described in the following sections:
> Online Methods: "Immunostaining of zebrafish embryos"; Supplementary Informati on: "Supplementary Table 4", p. 6.

10. Eukaryotic cell lines

a. State the source of each eukaryotic cell line used.

> No eukaryotic cell lines were used.

b. Describe the method of cell line authentication used.

> No eukaryotic cell lines were used.

c. Report whether the cell lines were tested for mycoplasma contamination.

> No eukaryotic cell lines were used.

d. If any of the cell lines used are listed in the database of commonly misidentified cell lines maintained by ICLAC, provide a scientific rationale for their use.

> No eukaryotic cell lines were used.

▶ Animals and human research participants

Policy information about studies involving animals; when reporting animal research, follow the ARRIVE guidelines

11. Description of research animals

Provide details on animals and/or animal-derived materials used in the study.

> Described in Online Methods: "Zebrafish embryo injections and imaging"

Policy information about studies involving human research participants

12. Description of human research participants

Describe the covariate-relevant population characteristics of the human research participants.

> Did not involve human research participants